Multimodal Longitudinal Optical Imaging Reveals Optic Neuritis Preceding Retinal Pathology in Experimental Autoimmune Encephalomyelitis

Raphael Raspe, Robert Günther, Ralf Uecker, Asylkhan Rakhymzhan, Friedemann Paul, Helena Radbruch, Raluca Aura Niesner,* and Anja Erika Hauser*

Correspondence
Prof. Hauser
anja.hauser-hankeln@charite.de

Abstract

Background and Objectives

Inflammatory demyelinating diseases of the CNS, chief among them multiple sclerosis (MS), are a major cause of disability in young adults. Early manifestations of MS commonly involve visual dysfunction, which is often caused by optic neuritis and is accompanied by quantifiable structural changes of the anterior visual pathway. Retinal optical coherence tomography (OCT) has emerged as an important tool for clinical assessment of these structural alterations, but the underlying pathobiological mechanisms and temporal dynamics are yet poorly understood at a cellular level.

Methods

Using the experimental autoimmune encephalomyelitis (EAE) model of MS in fluorescent reporter mouse strains for neuronal function and innate immune cells, we use a unique combination of retinal intravital 2-photon microscopy (2PM) and OCT. In this fashion, we elucidate the spatiotemporal interplay of functional and structural retinal changes over the course of 1 month after EAE induction, with histopathologic imaging validating main results.

Results

While all mice display histologic signs of optic neuritis early after EAE induction and independently of motor symptom severity, retinal signs of neuronal stress and parenchymal immune activation spike well after clinical peak of disease, with no signs of lasting structural damage appearing within 1 month after EAE induction. Thus, local retinal endpoints appear to be functions of downstream axonal damage rather than of immediate immune activation directed at the retina. However, as early as 1 week after EAE induction, retinal 2PM can detect recruitment of perivascular immune cells towards the optic nerve (ON), providing the earliest sign of disease activity in otherwise clinically inconspicuous mice.

Discussion

Our work identifies the recruitment of CX3CR1+ cells to the ON as an early sign of disease underlining the importance of combined structural and functional retinal imaging for the spatiotemporal characterization of neuroinflammatory and neurodegenerative processes. It further proposes retinal phagocyte orientation, morphology, and abundance as potential surrogate markers for neurodegenerative activity.

MORE ONLINE

Video

---

*These authors contributed equally to this work as senior authors.

From the Departments of Rheumatology and Clinical Immunology (R.R., A.E.H., R.U.) and Neuropathology (R.R., H.R.), Charité - Universitätsmedizin Berlin; Deutsches Rheuma-Forschungszentrum, a Leibniz Institute, Immune Dynamics (A.E.H., R.G.) and Biophysical Analytics (A.R., R.A.N.), Berlin; NeuroCure Clinical Research Center, Charité - Universitätsmedizin Berlin (F.P.), Experimental and Clinical Research Center, Charité - Universitätsmedizin Berlin and Max-Delbrueck Center for Molecular Medicine (F.P.); and Dynamic and Functional in vivo Imaging (R.A.N.) Freie Universität (R.A.N.) Berlin, Germany.

Glossary

2PM = 2-photon microscopy; **BSA** = Bovine serum albumin; **CFA** = complete Freund's adjuvant; **cSLO** = confocal scanning laser ophthalmoscopy; **ECi** = ethyl cinnamate; **EAE** = Experimental autoimmune encephalomyelitis; **ERG** = electroretinography; **GCIPL** = Ganglion cell and inner plexiform layer; **IRL** = inner retinal layers; **LSFM** = light sheet fluorescence microscopy; **MOG** = myelin oligodendrocyte glycoprotein; **NA** = numerical aperture; **ONH** = optic nerve head; **OCT** = optical coherence tomography; **OPO** = optical parametric oscillator; **PFA** = Paraformaldehyde; **PTX** = Pertussis toxin; **PBS** = phosphate-buffered saline; **pNF-H** = Phosphorylated neurofilament H; **PMT** = photomultiplier tube; **RGC** = retinal ganglion cell; **RNFL** = retinal nerve fiber layer; **SD-OCT** = spectral domain optical coherence tomography; **Srh 101** = Sulforhodamine 101; **Ti:Sa** = Titanium:Sapphire; **VEP** = visual evoked potentials.

Introduction

A common early clinical feature of multiple sclerosis (MS) is visual dysfunction, often caused by optic neuritis.[1] In trying to monitor anterior visual pathway affection and understand MS pathophysiology, the retina is considered a "window to the brain"[2] because it provides unique optical access to the CNS. Specifically, retinal optical coherence tomography (OCT) facilitates the observation of progressive retinal nerve fiber layer (RNFL) thinning as well as ganglion cell layer and inner plexiform layer (GCIPL) atrophy in MS—even at early disease stages without history of optic neuritis.[3-5] However, OCT alone cannot explain the cellular mechanisms behind these structural findings.

Histopathologic studies in MS mouse models, such as experimental autoimmune encephalomyelitis (EAE) induced by myelin oligodendrocyte glycoprotein peptide MOG$_{35-55}$ injection, have started to fill this gap. For example, inner retinal layer (IRL, = RNFL + GCIPL) thinning parallels retinal ganglion cells (RGC) loss, the axons of which form the RNFL and optic nerve (ON).[6-11] Retinal histology shows glial activation in EAE,[8,10-12] as confirmed in vivo by 2 recent studies using 2-dimensional static confocal scanning laser ophthalmoscopy (cSLO).[13,14]

Two-photon microscopy (2PM) is considered the gold standard for intravital, three-dimensional, time-resolved investigation of immune cell function,[15,16] and we have demonstrated the feasibility of time-resolved longitudinal retinal 2PM using an experimental autoimmune uveitis model.[17] Recently, we incorporated OCT into the same beam path, establishing near-instantaneous combined 2PM-OCT in mice.[18] Here, we use this unique approach to elucidate the spatiotemporal dynamics of immune cells, retinal neurons, and their interplay with the retinal microstructure and macrostructure over the first 4 weeks of MOG$_{35-55}$-induced EAE.

Methods

Standard Protocol Approvals

Animal experiments were approved by the appropriate state committees for animal welfare (G0074/17 and G0184/18, LAGeSo—Landesamt für Gesundheit und Soziales Berlin) and performed in accordance with current regulations.

Mice and EAE

We used 6–20-week-old mice bred in-house on a C57/Bl6-J background. *CerTNL-15* mice express TNL-15, a Förster resonance energy transfer (FRET)–based Ca^{2+}-biosensor, in Thy-1$^+$ neuronal populations, including RGCs.[19] Long-lasting intracellular calcium increases cause conformational changes of a troponin link, facilitating FRET from Cerulean (donor) to its conjoined Citrine (acceptor) molecule. Thus, the ratio of acceptor to donor fluorescence (FRET ratio) is indicative of intracellular calcium concentrations.[20] *CerTNL-15* mice were crossed to *LysM.tdRFP* mice expressing tdRFP in LysM$^+$ phagocytes.[21] Heterozygous *CX3CR1.EGFP*$^\pm$ mice express EGFP in monocytes, macrophages, and microglia.[22] EAE was induced and evaluated as previously described,[23] see supplementary eMethods.

Coregistered 2PM-OCT

Retinal 2PM was performed as previously described,[17] see supplementary eMethods. A maximum laser power of 30 mW was used to avoid photodamage, as discussed below. Spectral domain (SD-) OCT of the same volume was performed as previously described,[18] see supplementary eMethods. Maximum OCT laser power was below 1 mW.

Longitudinal Intravital Imaging

Two weeks before immunization, a titanium alloy head post was mounted onto the murine skull, allowing for fixation in our positioning system (Luigs & Neumann, Ratingen, Germany) built for translation along 3 axes and rotation around 2 axes with mechanical reproducibility of 2 μm, as previously described.[17] Mice were allowed to fully recover before commencing imaging. 2PM-OCT was performed 3 days before immunization, followed by 3 sessions before (days 7, 11, and 14) and 2 after clinical peak of disease (days 21 and 28). 2PM-OCT was performed under deep isoflurane inhalation anesthesia, which was added at 2% to oxygen for induction and reduced to approximately 1.5% for maintenance. After induction, the right eye was covered with ointment, while the left pupil was dilated using 2% phenylephrine and 0.4% tropicamide. In some *CX3CR1.EGFP*$^\pm$ mice, 50 μL of a sulforhodamine 101 solution were injected into the tail vein, staining blood vessels. The left pupil was positioned perpendicularly to the beam path, and a column of hydrogel (Vidisic, Bausch+Lomb, Germany) was applied. After mounting a planoconcave contact lens (3 mm diameter, −6 mm effective focal

length, Edmund Optics, Germany) to the pupil within the hydrogel, the objective was dipped into the hydrogel. Focal plane and field of view (FOV) were centered on the optic nerve head (ONH) using a built-in reflected-light fluorescence microscope. An OCT volume of 766 μm × 768 μm × 1,170 μm was acquired with 504 pixels × 505 pixels × 1,024 pixels digital resolution (total acquisition time: 105 seconds). The same FOV was imaged using 2PM with 240 μm depth, using a z-step of 10 μm (acquisition time: 82 seconds per z-stack). For *CerTNL-15 × LysM* mice, an initial z-stack was acquired using Cerulean/Citrine excitation and detection settings (see supplementary eMethods), followed by 20 z-stacks at 90 s/frame using tdRFP settings and, finally, a second Cerulean/Citrine z-stack. For *CX3CR1.EGFP*[±] mice, 20 z-stacks at 90 s/frame were acquired using EGFP/ sulforhodamine 101 settings. While the FOV remains stable for longer periods, we limited total anesthesia duration to 60 minutes per session to minimize stress.

Confocal and Light Sheet Fluorescence Microscopy (LSFM)

For tissue collection and staining protocols, see supplementary eMethods. Immunofluorescence-stained flat mounts were imaged using a Zeiss LSM 880 confocal microscope with a Plan-Apochromat 20x/NA 0.8 objective. Nine z-stacks of the IRL (FOV: 425.1 μm × 425.1 μm, z-step: 1 μm) were acquired for every flat mount, one centered on the ON head (ONH), as well as 4 in ONH-adjacent areas (= "central") and 4 in the retinal periphery (= "peripheral"), see eFigure 1H.

LSFM images of whole optic nerves were acquired using an Ultramicroscope II (LaVision BioTec—a Miltenyi company, Bielefeld, Germany) with a resolution of 0.271 μm/pixel. Each ON was acquired in toto using multiposition scans with an overlap of ~20% and z-step of 5 μm. Laser power was individually adjusted to avoid fluorophore saturation.

Data Analysis

Algorithms used for image postprocessing and analysis were written using existing plugins for FIJI, ImageJ 1.53t. For details on image analysis, see supplementary eMethods. Statistical analysis and graphical display were performed using GraphPad Prism (GraphPad, San Diego, CA). Schemes were created using BioRender (BioRender, Toronto, Canada). Figures were compiled using Microsoft PowerPoint for Microsoft 365 MSO Version 2310 (Microsoft, Redmond, WA, USA).

Data Availability

The datasets collected and analyzed in this study are available from the corresponding author on reasonable request.

Results

Optic Neuritis Occurs Independently of Paresis and Precedes Retinal Infiltration in EAE

After injection of MOG$_{35-55}$ peptide to elicit EAE, we monitored adolescent C57/Bl6-J mice of both sexes for up to 28 days. Motor function in EAE mice was moderately affected, with the median mouse (among those surveilled for 28 days) exhibiting tail paralysis and incomplete hind leg paresis. As previously described,[23] clinical disease peaked during the third week after induction (eFigure 1A). To verify uniform elicitation of optic neuritis, we quantified CD45$^+$ leukocyte numbers throughout the whole prechiasmatic ON using LSFM (eFigure 1, B and C). Compared with sham-immunized mice, mean leukocyte numbers in EAE mice were 26.2-fold higher at early time points (days 11–14; p = 0.0003) and 7.6-fold higher at day 28 postinduction (p < 0.0001). Furthermore, they increased 1.7-fold over the course of disease (Figure 1A; p = 0.0011). Importantly, ON infiltration at day 28 did not correlate with longitudinal severity of EAE-induced paralysis, rather, we observed an opposite (albeit not significant) tendency (r = −0.57, p = 0.09), with 2 motorically unaffected mice nevertheless exhibiting strong ON infiltration (Figure 1B, eTable 1 in the Supplement).

While the few leukocytes found in sham-immunized mice were mostly located in the outer regions of the nerve, i.e., closer to the vascularized perineurium, infiltrating leucocytes were found throughout the whole optic nerves of EAE mice, regardless of time point (eFigure 1D). Leukocytes within the ON of EAE mice formed more clusters early in disease (eFigure 1E, not significant), with 1.5-fold larger cluster sizes (eFigure 1F, p = 0.025). Conversely, leukocytes proved more evenly distributed at day 28 (eFigure 1G, p = 0.0007).

We next quantified CD45$^+$ leukocyte infiltration in retinal flat mounts (see eFigure 1, B and H). Whereas optic nerves already displayed heavy infiltration at early EAE stages, retinal infiltration increased significantly only at later time points (10.2-fold vs sham-immunized, p = 0.0004, Figure 1C, eFigure 1I). Importantly, with the focus of inflammation directed against the myelinated ON, we could observe 2.3 times less CD45$^+$ volume when shifting from the ONH outward to adjacent fields of view (p < 0.0001, Figure 1D).

We conclude that optic neuritis occurs independently of the display of motor symptoms and precedes retinal infiltration, which focuses mainly on the ONH.

Longitudinal Intravital Coregistered 2PM-OCT Serves to Study EAE Retinal Outcomes In Vivo

To investigate retrograde effects of EAE-induced optic neuritis on the retina, we used longitudinal intravital 2PM-OCT. eFigure 2A gives an overview of the experimental design used for intravital imaging and how measurements were grouped for analysis. A summary sketch of mouse positioning is shown in eFigure 2B, and eFigure 2C shows exemplary slices from three-dimensional volumes acquired with 2PM-OCT in 2 reporter mouse strains used in this study.

Limiting repeated imaging to the same eye, we used histologic analysis of retinal flat mounts from 2PM-exposed and

Figure 1 Optic Nerve and Retinal Leukocyte Infiltration
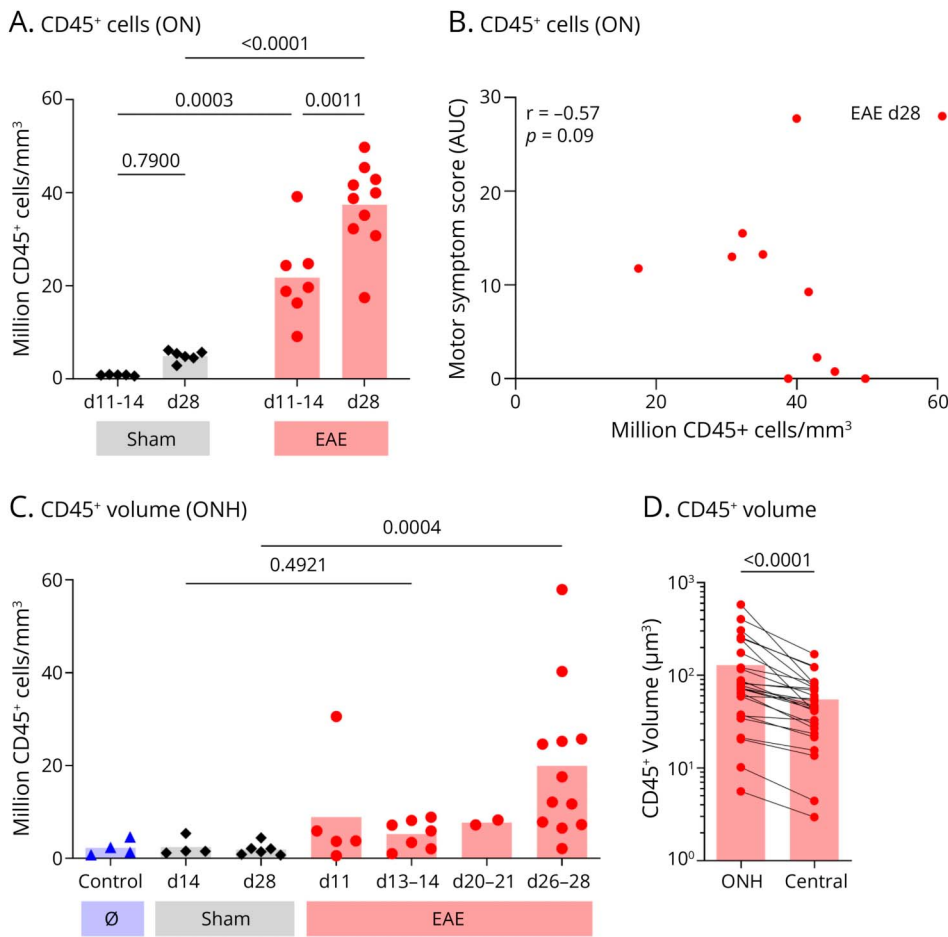
(A) Graph shows number of CD45+ cells per µm³ of ON for sham injected and EAE mice killed at the indicated days postinduction. (B) Graph shows correlation of CD45+ cell number in the ON (x axis) with AUC of longitudinally recorded motor symptom score of EAE mice (y axis). (C) Graph shows measurements of CD45+ volume in the ONH region of untreated control, sham-injected and EAE mice, the latter two having been sacrificed at the indicated days post-induction. (D) Graph shows measurements of CD45+ volume in ONH and adjacent central retinal areas of EAE mice, lines connect paired measurements in the same mouse. Individual datapoints represent means of measurements in left and right optic nerves/retinae. Bars in (A) and (C–D) represent means. Statistical significance was determined by repeated measures two-way analysis of variance with the subsequent Šídák multiple comparisons test in (A), two-tailed Spearman correlation in (B), the Kruskal-Wallis test with the subsequent Dunn multiple comparisons test in (C), and the 2-tailed Wilcoxon matched-pair signed-rank test in (D). AUC = area under the curve; EAE = experimental autoimmune encephalomyelitis; ON = optic nerve; ONH = optic nerve head.

nonexposed eyes to exclude effects of 2PM laser exposure on outcome parameters. We observed no significant differences in the staining patterns of phosphorylated neurofilament-H (pNF-H), which accumulates in proximal axons and somata of damaged neurons due to a breakdown of axonal transport,[24] CD45, as well as CX3CR1, a marker of microglia, monocytes, and macrophages (eFigure 2, D–J).

Thus, we reliably performed longitudinal 2PM-OCT in murine retinae without histologically evident photodamage.

Retinal Neurodegeneration Increases After EAE Peak and Features Prominently in Peripheral Areas

Using 2PM-OCT, we first studied signs of neuronal damage after optic neuritis. In OCT data, we bulk-segmented the IRL (eFigure 3A). Consistent with previous research,[6,13,25] we found that, whereas IRL thickness still increased over time in adolescent sham-immunized mice (mean Δ at day 21: +3.1 µm), it stagnated in EAE mice (mean Δ at day 21: +0.1 µm; $p < 0.0006$ for intercohort variance). The difference was more pronounced ($p < 0.0001$) in the retinal periphery and not significant ($p = 0.06$) in areas closer to the ONH (Figure 2A).

We next performed three-dimensional FRET-based RGC calcium imaging in *CerTN-L15* mice (Figure 2B) because sustained elevated calcium levels are indicative of neuronal stress preceding cell death.[23,26] FRET ratios remained stable during measurement periods exceeding 30 minutes, as previously published,[17] as well as over 28 days in sham-immunized mice (eFigure 3B), confirming the absence of imaging-induced neuronal stress. Comparing calcium levels in ONH-surrounding areas with baseline values, we observed only a modest, 5.3% increase of mean FRET ratio after clinical EAE peak ($p < 0.029$ vs healthy, Figure 2C, eFigure 3B), suggesting significant neuronal damage occurs in ONH-adjacent areas only at later disease stages.

To examine EAE-induced RGC loss more comprehensively, we quantified Brn3a+ RGCs in the retinal periphery using flat mounts (Figure 3A). Consistent with previous findings,[6,9,10] RGC counts in EAE mice were 27% lower than in sham-immunized mice at day 28 ($p = 0.0047$), whereas EAE mice at day 11–14 exhibited no significant RGC loss (Figure 3B).

We next counted pNF-H-accumulating RGC somata in flat mounts and quantified the extent of axonal pNF-H beading

Figure 2 Inner Retinal Layer Thickness and Neuronal Calcium Imaging
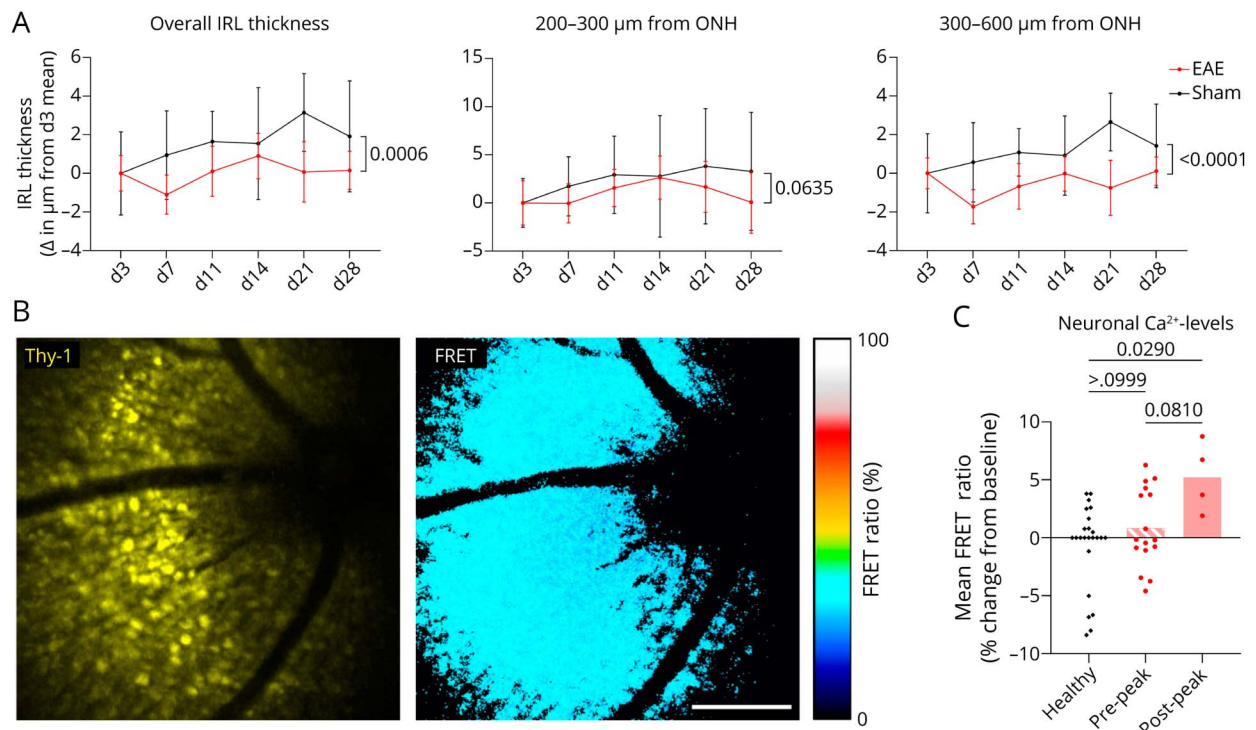
(A) Graphs show mean cumulative thickness of inner retinal layers (IRL), comprising retinal nerve fiber, ganglion cell, and inner plexiform layers. Left panel shows overall thickness measurements (200–600 μm from optic nerve head); middle and left panel show measurements at the more central (up to 300 μm from ONH) and more peripheral (300–600 μm from ONH) retinal regions, respectively. n = 9 mice for EAE (n = 5 remaining at day 28); n = 8 mice for sham-injected (n = 4 remaining at day 28). Bars represent 95% confidence intervals. Thickness is displayed as difference from baseline measurement at day 3 before induction. To better compare both cohorts, the respective mean of baseline measurements for each cohort was set to zero, all other measurements being normalized accordingly. Statistical significance was determined by ordinary 2-way analysis of variance, *p* values are reported for intercohort variation. (B) Representative 2PM image of Thy1+ RGC axons and somata (yellow, left panel) in a healthy mouse and graphical representation of the corresponding ratiometric FRET efficiency data after masking for Thy1+ pixels (right panel). Images are 3D projections of z-stacks. Scale bar represents 200 μm. (C) Graph shows change of mean ratiometric FRET efficiency compared with baseline measurements. Individual measurements are grouped as indicated in eFigure 2A. Bars represent means. Statistical significance was determined by the Kruskal-Wallis test with the subsequent Dunn multiple comparisons test. 2PM = 2-photon microscopy; EAE = experimental autoimmune encephalomyelitis; FRET = Förster resonance energy transfer; ONH = optic nerve head; RGC = retinal ganglion cell.

to assess still ongoing axonal damage. While healthy and sham-immunized mice displayed barely any pNF-H+ RGCs in the retinal periphery (mean: 0.5 cells/eye), they could readily be detected as early as days 13–14 post-EAE induction (mean: 13.6 cells/eye) but reached significantly elevated levels only on days 26–28 (mean: 30.1 cells/eye, *p* = 0.0023, Figure 3, A and C, eFigure 4A). At both timepoints, we found strong correlations between CD45+ ONH infiltration and the number of pNF-H+ RGCs in the periphery (early: *r* = 0.76, *p* = 0.004; late: *r* = 0.65, *p* = 0.001; eFigure 4B). Experimental autoimmune encephalomyelitis mice at day 28 postinduction scored 1.9-fold higher for axonal damage as indicated by axonal beading than sham-immunized mice (*p* = 0.0275, eFigure 4, C and D). Notably, pNF-H accumulation proved significantly more severe in the retinal periphery (*p* < 0.0001, Figure 3D, eFigure 4E) than in central areas.

We conclude that evidence of retinal neurodegeneration from intravital imaging and histology becomes significant only after clinical peak of EAE and is most pronounced in the retinal periphery.

Retinal Phagocyte Counts Surge After EAE Peak With No Distinct Patterns of Motility

We next examined retinal immune cells in EAE. Using 2PM-OCT in *LysM.tdRFP* mice,[21] we identified a population of resident LysM+ phagocytes surrounding the ONH of healthy mice (Figure 4A). While the number of LysM+ phagocytes in prepeak EAE mice was similar to healthy mice, it significantly increased after clinical peak of disease (1.5-fold vs healthy, *p* = 0.0047; 1.4-fold vs pre-peak EAE, *p* = 0.0412; Figure 4B, eFigure 5A).

Time-lapse imaging revealed a subset of motile phagocytes that, when overlayed with OCT imaging, seemed to be mostly travelling along retinal blood vessels (Figure 4C, Video 1). For technical reasons, the maximum cellular displacement rate we could resolve was ~30 μm/min. Thus, the observed movement along retinal blood vessels falls within the typical range of interstitial/perivascular rather than intraluminal cell velocity.[27,28] Automated cellular tracking revealed no significant difference in overall phagocyte motility between groups (mean aggregate displacement rate: 81.4 μm/min for healthy, 83.9 μm/min for prepeak, and 96.3 μm/min for post-peak EAE; Figure 4D, eFigure 5B). Assessing net migration along the

Figure 3 Histologic Evidence of Retinal Ganglion Cell Damage
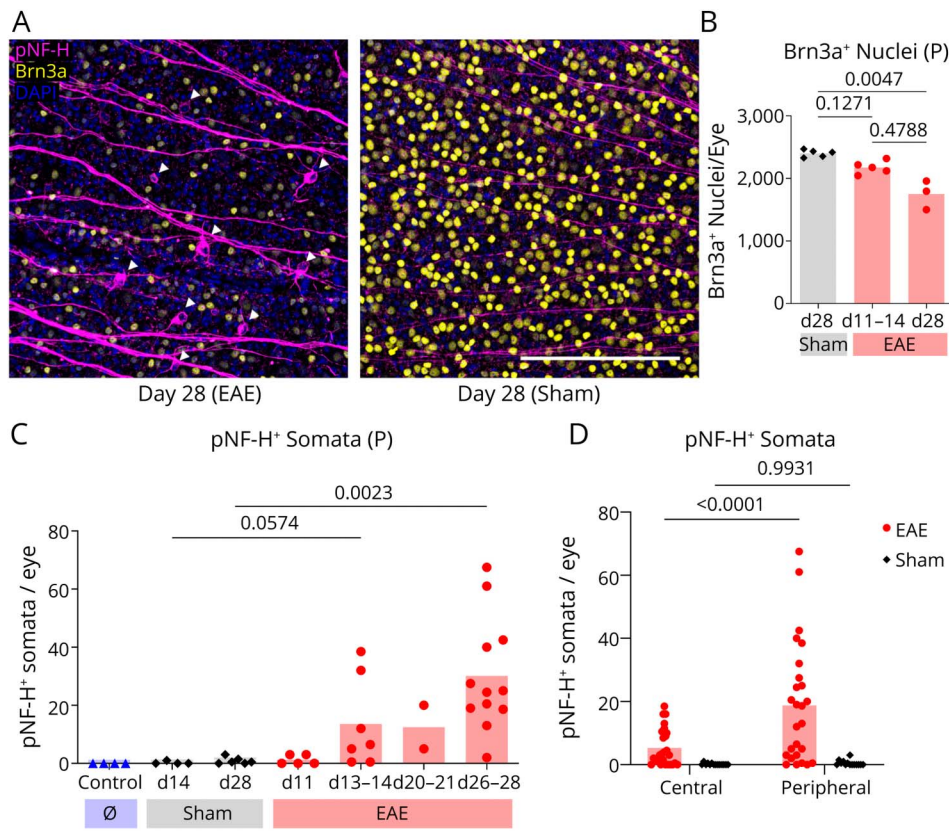
(A) Representative confocal microscopy images in retinal flat mounts, showing Brn3a$^+$ RGC nuclei (yellow) and somata and axons accumulating pNF-H (magenta) in the retinal periphery of a mouse undergoing EAE (left panel) and a sham-injected mouse (right panel) at day 28 postinduction. DAPI$^+$ nuclei are shown in blue. White arrowheads indicate RGC somata accumulating pNF-H. Images are maximum projections of z-stacks. Scale bar represents 200 μm. (B) Graph shows Brn3a$^+$ RGC nuclei counted in peripheral retinal areas. (C) Graph shows pNF-H$^+$ RGC somata counted per eye in peripheral retinal areas of untreated control, sham-injected, and EAE mice, the latter 2 having been killed at the indicated days postinjection. (D) Graph shows pNF-H$^+$ RGC somata counted in central and peripheral retinal area of the same mice. Datapoints in (B–D) represent means of measurements in left and right retina. Bars in (B–D) represent means. Statistical significance was determined by the Kruskal-Wallis test with subsequent Dunn multiple comparisons test in (B–C) and repeated measures 2-way analysis of variance with the subsequent Šídák multiple comparisons test in (D). EAE = experimental autoimmune encephalomyelitis; RGC = retinal ganglion cell.

centrifugal/centripetal axis (see eFigure 5C), we found balanced net migration of phagocytes towards the ONH and into the retinal periphery across all groups (mean aggregate centrifugal displacement: −0.5 μm/min for healthy, 1.0 μm/min for prepeak, and 2.3 μm/min for postpeak EAE; eFigure 5, D and E).

Taken together, retinal phagocyte numbers surge after EAE peak, without changes in motility or migratory patterns.

Retinal Microglia Display Strongest Signs of Activation After EAE Peak

To further characterize retinal innate immune cells in EAE, we used 2PM-OCT in *CX3CR1.EGFP* mice.[22] EAE mice exhibited a 1.4-fold higher density of CX3CR1$^+$ cells, i.e., microglia, macrophages, and monocytes, after clinical peak than healthy mice ($p = 0.02$, Figure 5, A and B, eFigure 6A).

Whereas in many contexts, activated macrophages tend to look amoeboid, retinal neurodegeneration produces "rod-shaped" microglia[29-31] that scavenge RGC debris and therefore align with axons.[32] Starting at day 21, elongated retinal microglia were detected in EAE mice. While some elongated cells were found to colocalize with Srh-101-stained vessels in all mice, overlaying 2PM and OCT data identified rod-shaped microglia stretching along nerve fibers in postpeak EAE mice (Figure 5C).

To quantify this effect, we used overall radial alignment of CX3CR1$^+$ cells (see supplementary eMethods) as a surrogate for alignment with nerve fibers which, like blood vessels, radially enter the ONH. Confirming this approach, the radially aligned fraction in perivascular cell surfaces, which are expected to be as aligned as the vessels, was 1.21-fold higher than in bona fide retinal cell surfaces ($p < 0.0001$, eFigure 6B). Consistent with qualitative observations, postpeak EAE mice displayed a significantly higher fraction of aligned CX3CR1$^+$ surfaces than both healthy and prepeak EAE mice (1.16-fold vs healthy, $p = 0.0003$; 1.11-fold vs pre-peak EAE, $p = 0.0197$; Figure 5D, eFigure 6C). Crucially, this appeared largely driven by bona fide retinal CX3CR1$^+$ cells (1.24-fold vs healthy, $p < 0.0001$; 1.19-fold vs prepeak EAE, $p = 0.0073$), while differences in the alignment of perivascular cells were less pronounced (Figure 5D, eFigure 6C), suggesting a major contribution of rod-shaped microglia attracted by axonal damage.

We conclude that significant morphological signs of resident microglia activation appear only after clinical peak of EAE.

Intravital Findings in CX3CR1.EGFP Mice Correlate Well With Results From Retinal Flat Mounts

We proceeded to confirm these findings with improved resolution in flat mounts. Consistent with intravital results, mean

Figure 4 In Vivo Retinal Phagocyte Quantification and Tracking
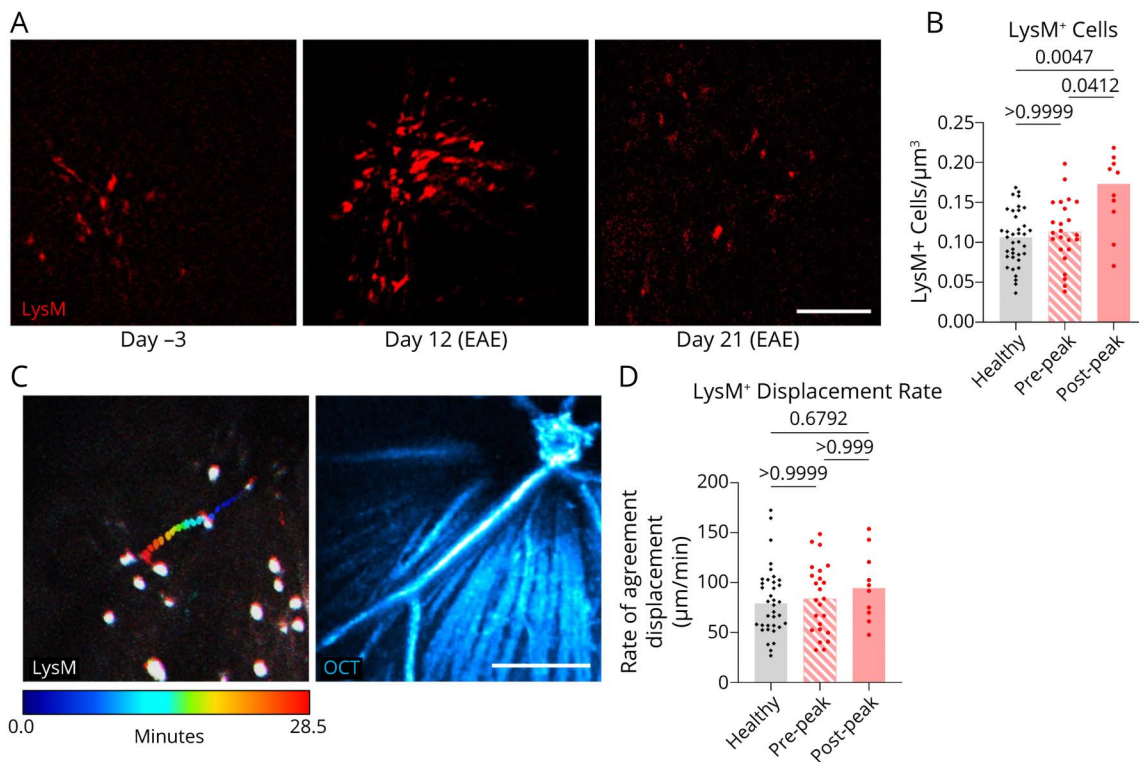
(A) Representative 2PM images of retinal LysM+ phagocytes (red) in the same mouse undergoing EAE at day 3 and 21 postinduction (left and middle), as well as a sham-treated mouse at day 21 postinjection. (B) Graph shows number of LysM+ phagocytes per μm^3. Individual measurements are grouped as indicated in eFigure 2A. (C) Left panel shows representative temporal color-coded display of a motile LysM+ cell in a healthy mouse before EAE induction. The right panel shows an en face projection of the RNFL, including the large retinal vessels, of the OCT volume acquired at the same timepoint. Same data as in Video 1. (D) Graph shows displacement rate of LysM+ cells. Individual datapoints represent aggregate displacement rate of all LysM+ cells registered over the course of one imaging session. Individual measurements are grouped as indicated in eFigure 2A. (A and C) show sum projections of z-stacks. Scale bars in (A and C) represent 200 μm. Bars in (B and D) represent means. Statistical significance was determined by the Kruskal-Wallis test with the subsequent Dunn multiple comparisons test. 2PM = 2-photon microscopy; EAE = experimental autoimmune encephalomyelitis; OCT = optical coherence tomography; RNFL = retinal nerve fiber layer.

CX3CR1+ volume per FOV was significantly higher in EAE than in sham-immunized mice at 26–28 days postinduction (eFigure 7A-C). In EAE mice, we additionally observed minute processes of retinal microglia—both rod-shaped and highly ramified ones—stretching along pNF-H+ axons that displayed heavy axonal beading. Such interactions were absent in sham-immunized mice (Figure 6A).

Next, we quantified the degree of radial orientation of CX3CR1+ cells in flat mounts. To once again validate our approach, we quantified the radial alignment of surfaces using stains of different cellular structures in the same healthy flat mount, with low alignment expected for Brn3a+ and high alignment expected for pNF-H+ surfaces (Figure 3A). Indeed, pNF-H+ surfaces exhibited a 1.86-fold higher aligned fraction ($p = 0.0034$, eFigure 7D).

Confirming our in vivo findings, the aligned fraction of CX3CR1+ surfaces increased over time in EAE mice, reaching 1.19-fold higher values than in sham-immunized mice at d26-28 postimmunization ($p = 0.0036$, Figure 6B, eFigure 7E).

Importantly, we found robust correlations of intravital data with flat mount data for both CX3CR1+ volume ($r = 0.71$, $p = 0.03$; Figure 6C) and radial alignment ($r = 0.79$, $p = 0.01$; Figure 6D), confirming that intravital 2PM preserves clinically relevant information.

Highly Motile Perivascular CX3CR1+ Cells Preferentially Migrate Toward the ONH in Early EAE

Time-lapse imaging identified some motile CX3CR1+ cells, virtually all of them round, migrating along Srh101-stained retinal vessels (Figure 7A, Video 2). We sporadically observed tissue surveillance by non-migratory CX3CR1+ cells dynamically extending and retracting their processes (eFigure 8A). While automated tracking was technically limited to maximum displacement rates of ~30 μm/min, we occasionally detected cellular movement across consecutive slices of one z-stack (acquired at ~3.3 seconds per slice) with speeds of ~15 μm/s (eFigure 8B), within the range of leukocyte rolling inside vessels.[33] Accordingly, such movement was exclusively observed along vessels.

**Figure 5** In Vivo Retinal CX3CR1+ Cell Quantification
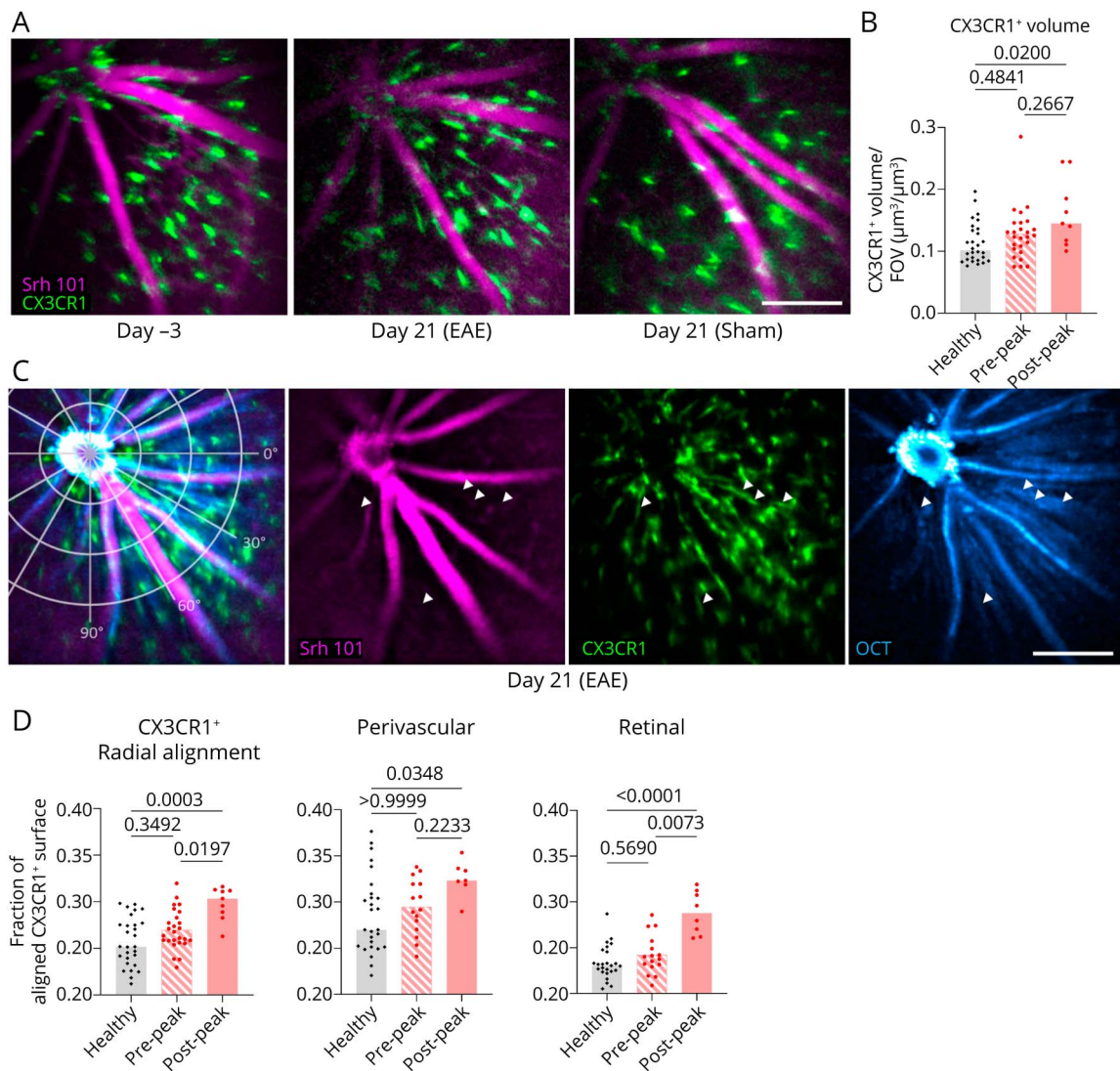
(A) Representative 2PM images of the same mouse undergoing EAE at days 3 and 21 postinduction (left and middle), as well as a sham-injected littermate at day 21. (B) Graph shows measurements of CX3CR1$^+$ volume per μm³ of field of view (FOV). Individual measurements are grouped as indicated in eFigure 2A. (C) Representative 2PM and en face OCT image of an EAE mouse at day 21 postinduction. The left panel shows superimposition of the 3 panels to the right, a superimposed polar coordinate system with the ONH as pole serves as reference for subsequent radial alignment measurements. White arrowheads in the 3 panels to the right indicate positions of rod-shaped microglia that are aligned with nerve fibers. (D) Graphs show radial alignment measurements of CX3CR1$^+$ surface edges. The left panel shows overall radial alignment; middle and left panels show radial alignment of perivascular macrophages (defined by a distance of ≤ 10 μm from blood vessels) and retinal (defined by a distance of > 10 μm from blood vessels) microglia, respectively. Individual measurements are grouped as indicated in eFigure 2A. (A and C) show sum projections of z-stacks. Scale bars in (A and C) represent 200 μm. Bars in (B and D) represent means. Blood vessels in (A and C), stained with sulforhodamine 101 (Srh 101), are shown in magenta, CX3CR1$^+$ cells are shown in green. OCT intensity values in (C) are displayed in shades of cyan. Statistical significance was determined by the Kruskal-Wallis test with the subsequent Dunn multiple comparisons test. 2PM = 2-photon microscopy; EAE = experimental autoimmune encephalomyelitis; OCT = optical coherence tomography; ONH = optic nerve head.

Automated tracking revealed markedly increased CX3CR1$^+$ cell motility in EAE mice. Contrasting all other observed outcome parameters, motility was highest before clinical EAE peak (mean aggregate displacement rate: 13.6 μm/min for healthy, 65.9 μm/min for prepeak, 30.3 μm/min for post-peak EAE; p = 0.0006 for prepeak EAE vs healthy; Figure 7B, eFigure 8D). Moreover, while CX3CR1$^+$ cells displayed no directional bias in healthy and postpeak EAE mice, they significantly favored ONH-directed migration before peak (eFigure 8E). Analysis of individual prepeak time points showed this was almost exclusively driven by ONH-directed

migration at day 7, our earliest follow-up after EAE induction (mean aggregate ONH-directed displacement for day 7 EAE: 17.2 μm/min; p = 0.0486 vs day 7 healthy; Figure 7, C and D, Videos 3 and 4).

Incidentally, most individual vessels were "two-way streets," with both centrifugal and centripetal movement detected along the same vessels (Figure 7D, Video 4). Perivascular cells travelled 1.2-fold longer overall distances (p = 0.0091; eFigure 8F) and 1.6-fold longer radial distances (p < 0.0001; eFigure 8G) than those within the tissue.

Figure 6 CX3CR1+ Cell Quantification in Retinal Flat Mounts
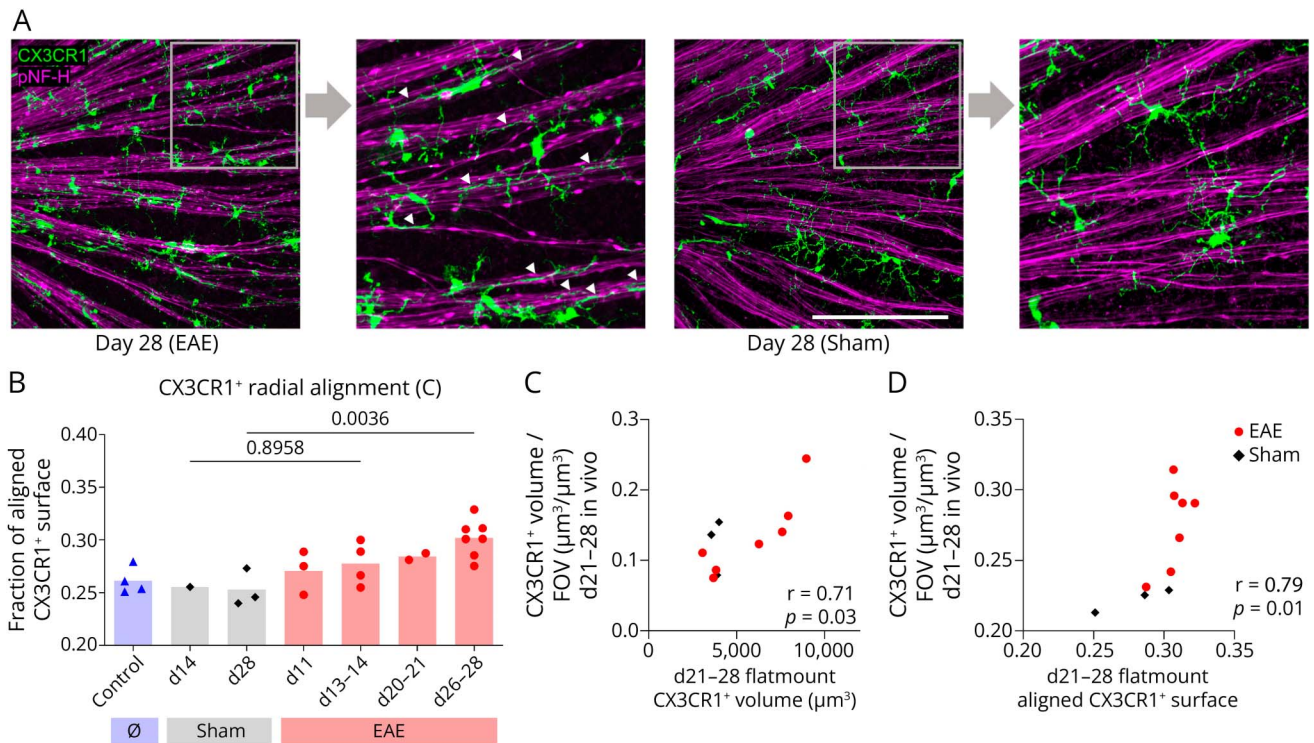
(A) Confocal microscopy images acquired in central retinal flat mount areas in representative EAE and sham injected mice at 28 days postinduction. CX3CR1⁺ microglia, monocytes, and macrophages are shown in green, pNF-H⁺ axons of retinal ganglion cells are shown in magenta. The area contained in the white overlayed square in the left image of each panel is magnified in the right image. White arrowheads indicate microglial processes aligned with axons. Scale bar represents 200 µm. Images are maximum projections of z-stacks. (B) Graph shows radial alignment measurements of CX3CR1⁺ surface edges in central retinal flatmount areas for untreated control, sham-injected, and EAE mice, the latter 2 having been sacrificed at the indicated days postinduction. Edge voxels are considered aligned if the spatial orientation of the respective edge differs less than ±20° from the polar angle of the edge, using a polar coordinate system with the optic nerve head (ONH) as pole for reference (as illustrated in Figure 5C). (C) Graph shows correlation of CX3CR1⁺ volume as measured postmortem in flat mounts (x axis) with CX3CR1⁺ volume as measured in vivo immediately before death (y axis) for mice sacrificed after clinical peak of EAE (days 21–28). (D) Graph shows correlation of CX3CR1⁺ radial alignment as measured postmortem in flat mounts (x axis) with CX3CR1⁺ radial alignment as measured in vivo immediately before death (y axis) for mice sacrificed after clinical peak of EAE (days 21–28). Datapoints in (B) represent means of measurements in left and right retina. Bars in (B) represent means. Statistical significance was determined by the Kruskal-Wallis-Test with the subsequent Dunn multiple comparisons test in B, and 2-tailed Spearman correlation in (C–D). EAE = experimental autoimmune encephalomyelitis.

In summary, increased CX3CR1⁺ cell motility and migration toward the ONH seem to be very early markers of disease activity.

Discussion

While OCT has been clinically established in MS for some years, few studies have explored the pathogenesis of retinal changes in EAE,[6-12] and studies using longitudinal intravital imaging have been exceedingly rare,[13,14] leaving the exact spatiotemporal progress of retinal outcomes mainly obscure. Our work uniquely combines the safe retinal use of 2PM, the gold standard for intravital, functional cellular imaging, with SD-OCT to characterize the time-resolved dynamics of retinal immune cell activation in EAE in relation to the retinal macrostructure and microstructure. Crucially, intravital findings correlated well with data acquired in retinal flat mounts—even in the case of CX3CR1⁺ cells, which are notoriously hard to resolve because of their minute processes.

MOG-EAE proved an ideal model to investigate optic neuritis and its retrograde retinal effects, as virtually all mice injected with MOG₃₅-₅₅, even those that never displayed any clinical signs of transverse myelitis, developed optic neuritis as evidenced by CD45⁺ ON infiltration. This can be attributed to considerably higher MOG expression in the murine ON than in the spinal cord, a fact that also accounts for substantial rates of spontaneous optic neuritis in mice expressing a transgenic MOG-specific T-cell receptor.[34]

Using intravital retinal imaging, we identified ONH-directed perivascular immune cell recruitment as the earliest observable sign of incipient optic neuritis. Indeed, ON pathology occurs at least several days before the retinal tissue itself displays any signs of either immune activation or neuronal stress. While CD45⁺ infiltration of optic nerves occurred as early as 11 days postimmunization, retinal infiltration was significantly elevated only after clinical EAE peak and concentrated around the ONH—unlike retinal periphlebitis in MS, which is characterized by CD45⁺ aggregates surrounding peripheral retinal vessels.[35]

Figure 7 In Vivo Retinal CX3CR1+ Cell Tracking
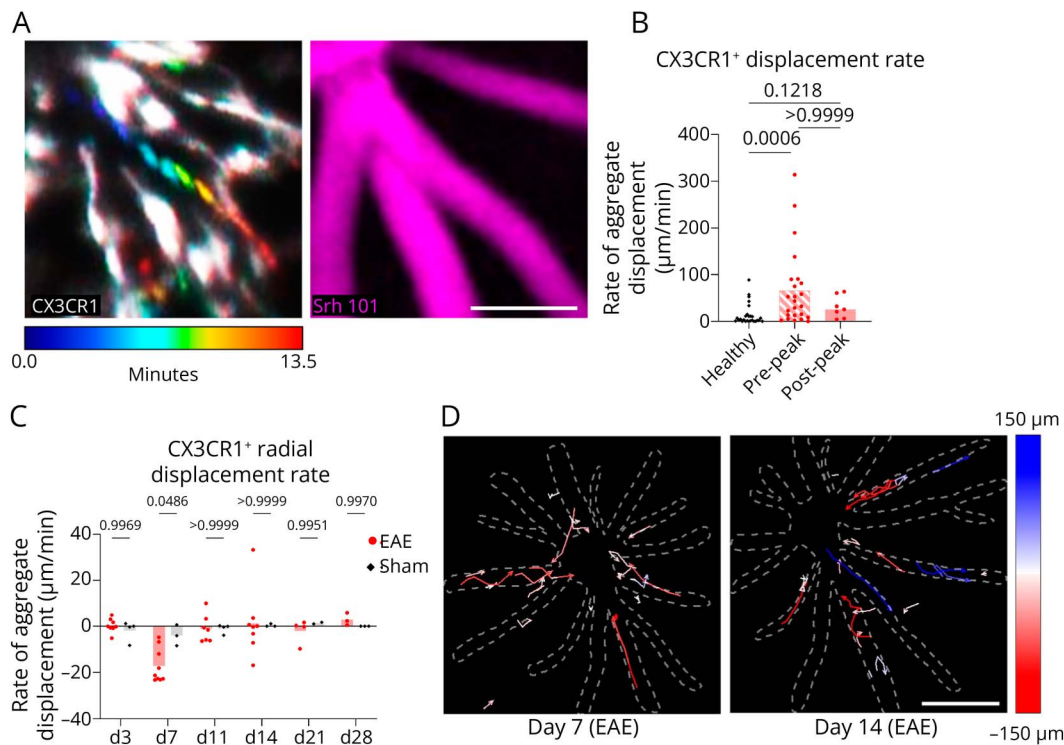
(A) Left panel shows representative temporal color-coded display of a motile CX3CR1[+] cell in an EAE mouse at day 14 postinduction, acquired using 2PM. Right panel shows corresponding retinal vessels stained with sulforhodamine 101 (Srh 101). Same data as in Video 2. (B) Graph shows displacement rate of CX3CR1^{+} cells. Individual datapoints represent aggregate displacement rate of all CX3CR1^{+} cells registered over the course one imaging session. Individual measurements are grouped as indicated in eFigure 2A. (C) Graph shows radial displacement rate of CX3CR1^{+} cells. Individual datapoints represent aggregate radial displacement rate of all CX3CR1^{+} cells registered over the course one imaging session. (D) CX3CR1[+] single-cell tracks detected in measurements at days 7 (left panel) and 14 (right panel) in the same EAE mouse. Tracks are colored according to their radial displacement (see color bar, negative values represent movement toward the optic nerve (ON) head, positive values represent movement toward the periphery). Dashed lines represent blood vessel outlines. Same data as in Videos 3 and 4. Scale bar in (A) represents 50 μm. Scale bar in (D) represents 200 μm. Bars in represent means. Statistical significance was determined by the Kruskal-Wallis test with the subsequent Dunn multiple comparisons test in (B) and ordinary 2-way analysis of variance with the subsequent Šídák multiple comparison test in (D). 2PM = 2-photon microscopy; EAE =experimental autoimmune encephalomyelitis.

Importantly, RGC axons leave the retina still unmyelinated. Retinal infiltration in EAE thus seems to mainly represent spill-over from the myelin-directed immune response taking place in the ON.

Conversely, signs of axonal damage, reflected in accumulation of pNF-H in axonal beads and RGC somata, were highest in the periphery. Possibly, the axons of peripheral RGCs are most prone to disruption of axonal transport—of which pNF-H accumulation is reflective—because they travel the longest distances. Preferential affection of peripheral RGCs might explain why we detected only modest increases in intracellular RGC calcium around the ONH, which we needed as a landmark for repeated imaging. Furthermore, previous studies have revealed neurodegenerative retinal remodeling occurring for several months after induction of EAE.[6] A future study with a decidedly longer follow-up period could more comprehensively investigate the spatiotemporal dynamics of EAE-related neurodegeneration, possibly including reporter mice for intravital visualization of axonal transport, such as Thy1-CFP-MitoC mice containing fluorescently labelled neuronal mitochondria.[36]

To our knowledge, only 2 previous studies have longitudinally and intravitally investigated retinal innate immune cells in EAE.[13,14] Paralleling our own results, both noted an increase in CX3CR1[+] cell density peaking at the onset of clinical remission, well after clinical EAE peak. Since neither performed time-resolved imaging, the early recruitment of CX3CR1^{+} cells to the ON observed herein eluded them. Further research is needed to clarify the nature of these cells. Microglia characteristically express CX3CR1, but so do monocytes and perivascular macrophages—and even some effector T-cell subsets.[37,38] The round phenotype of migrating cells and their perivascular location suggest they might not be resident retinal microglia but rather perivascular macrophages or altogether transiting cells. Indeed, outcomes that can be more confidently ascribed to resident microglia activation—like increased overall CX3CR1[+] cellular density and orientation of rod-shaped cells along nerve fibers—were seen after clinical peak, when CX3CR1[+] ONH-directed migration had already ceased. The tendency of rod-shaped microglia to interact with already damaged axons[29-31] suggests that, in EAE, retinal microglia are primarily reacting to axonal damage and—at least at these early stages of disease—not themselves driving neurodegeneration.

Integrating the chronological sequence of our observations with previously published findings, we propose a model in which optic neuritis in MOG-EAE precedes retrograde axonal degeneration and RGC loss, which in turn trigger resident innate immune cell activation. The earliest events we observed—both indicative of optic neuritis—were recruitment of CX3CR1+ cells to the ON exclusively at day 7, and CD45+ ON infiltration detected at day 11. Histologic RGC affection seems to follow swiftly, with a recent study describing synaptic loss at day 12, before onset of paralytic symptoms.[39] Correspondingly, we found first, if not significant, signs of pNF-H+ accumulation in RGC somata at days 13–14—but, importantly, not at day 11, when optic neuritis was already showing. Further research could determine the exact tipping point at which RGC loss becomes inevitable. Once this point is reached, resident microglia start disposing of dead or dying RGCs, as evidenced by increased CX3CR1+ cell density and occurrence of rod-shaped microglia after 3 weeks of EAE. Whether microglial activation subsides after acute optic neuritis or drives prolonged, excessive retinal neurodegeneration warrants further investigation.

As for longitudinal assessments of visual function, optokinetic reflex measurements display first signs of reduced visual acuity as the second week of EAE ends.[9] As discussed above, this coincides with earliest histologic affection of RGCs, suggesting deteriorating RGC function is what reduces visual acuity. Longitudinal electrophysiologic study of the visual system in early murine EAE has been rare, yielding conflicting results. Both delayed signal latency in visual evoked potential (VEP) measurements, reflective of demyelination, and amplitude reduction in electroretinography (ERG), suggestive of already full-blown RGC dysfunction or loss, have been documented as early as day 7.[40] However, in another study, ERG was not significantly altered until later, postacute stages, with VEP already previously affected.[41] Ideally, future studies could combine 2PM-OCT with longitudinal investigation of functional visual outcomes to help disentangle the chronological sequence of early visual impairment and underlying cellular mechanisms.

Coupling OCT into the beam path proved essential to assess cellular interaction with nerve fibers and blood vessels even in absence of specific fluorescent stains. Its main purpose, however, is to measure IRL thickness, which provides a relatively reliable measure of retrograde retinal changes following ON damage.[6,42] Compared with adolescent sham-immunized mice, which displayed residual IRL-thickening, IRL thickness stagnated in EAE mice, as has been described before in early EAE.[6] However, this might be a function of disease-related wasting—like weight loss at symptom onset—rather than a specific sign of neuronal stress. 2PM-OCT technically allows for colocalization of 2PM and OCT data on a pixel-by-pixel basis. Given that the greater part of IRL thinning happens during clinical remission,[6,13,43] our follow-up period of 28 days did not suffice to register meaningful overall, let alone pixel-wise, IRL thinning in OCT data. Extending the follow-up period in future studies and using AI-based instruments for

detection of subtler differences could yield meaningful pixel-by-pixel correlations of structural OCT with functional 2PM data. Future applications of our setup could also include doppler OCT, which would, among other things, allow for the differentiation of arterial and venous vessels,[44] or OCT angiography to monitor blood-retina-barrier integrity.[45]

Laser microscopy of the retina is limited by the low retinal threshold for phototoxicity. Importantly, using the settings specified above we could detect no adverse effects: All outcomes analyzed in this study remained stable in healthy mice, both during prolonged imaging sessions, as well as over multiple consecutive sessions. Repeatedly 2PM-exposed eyes were histologically indistinguishable from nonexposed eyes of the same mice. Thus—while laser energy levels exceeded the justifiably cautious limits for human retinal imaging—our murine setup worked safely, without imaging-induced artifacts. Our approach would easily lend itself to application in a variety of mouse models for other neurodegenerative conditions with a known retinal co-affection, including models for Alzheimer[46] and Parkinson[47] disease as well as post-ischemic neurodegeneration.[48]

Next to 2PM, other optical imaging techniques have been developed to longitudinally study retinal immune cells. In particular, combining cSLO with adaptive optics (AO-SLO) has expanded its utility to include three-dimensional and time-resolved imaging.[49,50] While 2PM intrinsically enables three-dimensional imaging deep within the tissue,[15] three-dimensional AO-SLO requires coregistration with OCT for focal depth calibration.[49,50] Adaptive optics may provide higher spatial resolution because they continuously correct system-inherent and tissue-inherent wavefront distortions, but their application requires more technical know-how and accordingly seems more challenging than the approach presented in this study. Scientists studying retinal outcomes intravitally can choose the method that best suits their requirements concerning imaging depth, FOV, spatial and temporal resolution. In our case, 2PM-OCT proved suitable both for detection of very early signs of disease—crucial for designing strategies of early interception—as well as for monitoring retinal neurodegeneration and consecutive resident immune cell activation, providing important insight into overall disease activity at later stages.

Acknowledgment

Study Funding

Disclosure

Publication History

Appendix Authors

Name	Location	Contribution
Raphael Raspe	Departments of Neuropathology, and Rheumatology and Clinical Immunology, Charité - Universitätsmedizin Berlin; Immune Dynamics, Deutsches Rheuma-Forschungszentrum (DRFZ), a Leibniz Institute	Drafting/revision of the manuscript for content, including medical writing for content; major role in the acquisition of data; study concept or design; analysis or interpretation of data
Robert Günther	Immune Dynamics, Deutsches Rheuma-Forschungszentrum (DRFZ), a Leibniz Institute	Major role in the acquisition of data
Ralf Uecker	Immune Dynamics, Deutsches Rheuma-Forschungszentrum (DRFZ), a Leibniz Institute	Major role in the acquisition of data
Asylkhan Rakhymzhan	Biophysical Analytics, Deutsches Rheuma-Forschungszentrum (DRFZ), a Leibniz Institute	Major role in the acquisition of data
Friedemann Paul	NeuroCure Clinical Research Center, Charité - Universitätsmedizin Berlin; Experimental and Clinical Research Center, Charité - Universitätsmedizin Berlin and Max Delbrueck Center for Molecular Medicine, Berlin	Drafting/revision of the manuscript for content, including medical writing for content; study concept or design; analysis or interpretation of data
Helena Radbruch	Department of Neuropathology, Charité - Universitätsmedizin Berlin	Drafting/revision of the manuscript for content, including medical writing for content; study concept or design; analysis or interpretation of data
Raluca Aura Niesner	Biophysical Analytics, Deutsches Rheuma-Forschungszentrum (DRFZ), a Leibniz Institute; Dynamic and Functional in vivo Imaging, Freie Universität Berlin	Drafting/revision of the manuscript for content, including medical writing for content; study concept or design; analysis or interpretation of data; additional contributions (in addition to one or more of the above criteria)
Anja Erika Hauser	Department of Rheumatology and Clinical Immunology, Charité - Universitätsmedizin Berlin; Immune Dynamics, Deutsches Rheuma-Forschungszentrum (DRFZ), a Leibniz Institute	Drafting/revision of the manuscript for content, including medical writing for content; study concept or design; analysis or interpretation of data

References

1. Petzold A, Fraser CL, Abegg M, et al. Diagnosis and classification of optic neuritis. *Lancet Neurol*. 2022;21(12):1120-1134. doi:10.1016/S1474-4422(22)00200-9
2. London A, Benhar I, Schwartz M. The retina as a window to the brain-from eye research to CNS disorders. *Nat Rev Neurol*. 2013;9(1):44-53. doi:10.1038/nrneurol.2012.227
3. Martinez-Lapiscina EH, Arnow S, Wilson JA, et al. Retinal thickness measured with optical coherence tomography and risk of disability worsening in multiple sclerosis: a cohort study. *Lancet Neurol*. 2016;15(6):574-584. doi:10.1016/S1474-4422(16)00068-5
4. Petzold A, Balcer LJ, Calabresi PA, et al. Retinal layer segmentation in multiple sclerosis: a systematic review and meta-analysis. *Lancet Neurol*. 2017;16(10):797-812. doi:10.1016/S1474-4422(17)30278-8
5. Lin T-Y, Vitkova V, Asseyer S, et al. Increased serum neurofilament light and thin ganglion cell-inner plexiform layer are additive risk factors for disease activity in early multiple sclerosis. *Neurol Neuroimmunol Neuroinflamm*. 2021;8(5):e1051. doi:10.1212/NXI.0000000000001051
6. Cruz-Herranz A, Dietrich M, Hilla AM, et al. Monitoring retinal changes with optical coherence tomography predicts neuronal loss in experimental autoimmune encephalomyelitis. *J Neuroinflammation*. 2019;16(1):203. doi:10.1186/s12974-019-1583-4
7. Brambilla R, Dvoriantchikova G, Barakat D, Ivanov D, Bethea JR, Shestopalov VI. Transgenic inhibition of astroglial NF-κB protects from optic nerve damage and retinal ganglion cell loss in experimental optic neuritis. *J Neuroinflammation*. 2012;9:213. doi:10.1186/1742-2094-9-213
8. Horstmann L, Kuehn S, Pedreiturria X, et al. Microglia response in retina and optic nerve in chronic experimental autoimmune encephalomyelitis. *J Neuroimmunol*. 2016;298:32-41. doi:10.1016/j.jneuroim.2016.06.008
9. Larabee CM, Desai S, Agasing A, et al. Loss of Nrf2 exacerbates the visual deficits and optic neuritis elicited by experimental autoimmune encephalomyelitis. *Mol Vis*. 2016;22:1503-1513.
10. Jin J, Smith MD, Kersbergen CJ, et al. Glial pathology and retinal neurotoxicity in the anterior visual pathway in experimental autoimmune encephalomyelitis. *Acta Neuropathol Commun*. 2019;7(1):125. doi:10.1186/s40478-019-0767-6
11. Gharagozloo M, Smith MD, Jin J, et al. Complement component 3 from astrocytes mediates retinal ganglion cell loss during neuroinflammation. *Acta Neuropathologica*. 2021;142(5):899-915. doi:10.1007/s00401-021-02366-4
12. Maisam Afzali A, Stüve L, Pfaller M, et al. Aquaporin-4 prevents exaggerated astrocytosis and structural damage in retinal inflammation. *J Mol Med (Berl)*. 2022;100(6):933-946. doi:10.1007/s00109-022-02202-6
13. Frenger MJ, Hecker C, Sindi M, et al. Semi-automated live tracking of microglial activation in CX3CR1GFP mice during experimental autoimmune encephalomyelitis by confocal scanning laser ophthalmoscopy. *Front Immunol*. 2021;12:761776. doi:10.3389/fimmu.2021.761776
14. Cruz-Herranz A, Oertel FC, Kim K, et al. Distinctive waves of innate immune response in the retina in experimental autoimmune encephalomyelitis. *JCI Insight*. 2021;6(11):e149228. doi:10.1172/jci.insight.149228
15. Germain RN, Robey EA, Cahalan MD. A decade of imaging cellular motility and interaction dynamics in the immune system. *Science*. 2012;336(6089):1676-1681. doi:10.1126/science.1221063
16. Niesner RA, Hauser AE. Recent advances in dynamic intravital multi-photon microscopy. *Cytometry A*. 2011;79(10):789-798. doi:10.1002/cyto.a.21140
17. Bremer D, Pache F, Gunther R, et al. Longitudinal intravital imaging of the retina reveals long-term dynamics of immune infiltration and its effects on the glial network in experimental autoimmune uveoretinitis, without evident signs of neuronal dysfunction in the ganglion cell layer. *Front Immunol*. 2016;7:642. doi:10.3389/fimmu.2016.00642
18. Rakhymzhan A, Reuter L, Raspe R, et al. Coregistered spectral optical coherence tomography and two-photon microscopy for multimodal near-instantaneous deep-tissue imaging. *Cytometry A*. 2020;97(5):515-527. doi:10.1002/cyto.a.24012
19. Heim N, Garaschuk O, Friedrich MW, et al. Improved calcium imaging in transgenic mice expressing a troponin C-based biosensor. *Nat Methods*. 2007;4(2):127-129. doi:10.1038/nmeth1009
20. Rinnenthal JL, Börnchen C, Radbruch H, et al. Parallelized TCSPC for dynamic intravital fluorescence lifetime imaging: quantifying neuronal dysfunction in neuroinflammation. *PLoS One*. 2013;8(4):e60100. doi:10.1371/journal.pone.0060100
21. Clausen BE, Burkhardt C, Reith W, Renkawitz R, Förster I. Conditional gene targeting in macrophages and granulocytes using LysMcre mice. *Transgenic Res*. 1999;8(4):265-277. doi:10.1023/a:1008942828960
22. Jung S, Aliberti J, Graemmel P, et al. Analysis of Fractalkine receptor CX(3)CR1 function by targeted deletion and green fluorescent protein reporter gene insertion. *Mol Cell Biol*. 2000;20(11):4106-4114. doi:10.1128/MCB.20.11.4106-4114.2000
23. Siffrin V, Radbruch H, Glumm R, et al. In vivo imaging of partially reversible th17 cell-induced neuronal dysfunction in the course of encephalomyelitis. *Immunity*. 2010;33(3):424-436. doi:10.1016/j.immuni.2010.08.018
24. Petzold A. Neurofilament phosphoforms: surrogate markers for axonal injury, degeneration and loss. *J Neurol Sci*. 2005;233(1-2):183-198. doi:10.1016/j.jns.2005.03.015
25. Nishioka C, Liang H-F, Barsamian B, Sun S-W. Sequential phases of RGC axonal and somatic injury in EAE mice examined using DTI and OCT. *Mult Scler Relat Disord*. 2019;27:315-323. doi:10.1016/j.msard.2018.11.010
26. Mossakowski AA, Pohlan J, Bremer D, et al. Tracking CNS and systemic sources of oxidative stress during the course of chronic neuroinflammation. *Acta Neuropathologica*. 2015;130(6):799-814. doi:10.1007/s00401-015-1497-x

27. Khandoga AG, Khandoga A, Reichel CA, Bihari P, Rehberg M, Krombach F. In vivo imaging and quantitative analysis of leukocyte directional migration and polarization in inflamed tissue. *PLoS One*. 2009;4(3):e4693. doi:10.1371/journal.pone.0004693

28. Stark K, Eckart A, Haidari S, et al. Capillary and arteriolar pericytes attract innate leukocytes exiting through venules and 'instruct' them with pattern-recognition and motility programs. *Nat Immunol*. 2013;14(1):41-51. doi:10.1038/ni.2477

29. Ziebell JM, Taylor SE, Cao T, Harrison JL, Lifshitz J. Rod microglia: elongation, alignment, and coupling to form trains across the somatosensory cortex after experimental diffuse brain injury. *J Neuroinflammation*. 2012;9:247. doi:10.1186/1742-2094-9-247

30. de Hoz R, Gallego BI, Ramírez AI, et al. Rod-like microglia are restricted to eyes with laser-induced ocular hypertension but absent from the microglial changes in the contralateral untreated eye. *PLoS One*.2013;8(12):e83733. doi:10.1371/journal.pone.0083733

31. Yuan T-F, Liang Y-X, Peng B, Lin B, So K-F. Local proliferation is the main source of rod microglia after optic nerve transection. *Sci Rep*. 2015;5:10788. doi:10.1038/srep10788

32. Zhang Y, Peng B, Wang S, et al. Image processing methods to elucidate spatial characteristics of retinal microglia after optic nerve transection. *Sci Rep*. 2016;6:21816. doi:10.1038/srep21816

33. Dunne JL, Ballantyne CM, Beaudet AL, Ley K. Control of leukocyte rolling velocity in TNF-alpha-induced inflammation by LFA-1 and Mac-1. *Blood*. 2002;99(1):336-341. doi:10.1182/blood.v99.1.336

34. Bettelli E, Pagany M, Weiner HL, Linington C, Sobel RA, Kuchroo VK. Myelin oligodendrocyte glycoprotein-specific T cell receptor transgenic mice develop spontaneous autoimmune optic neuritis. *J Exp Med*. 2003;197(9):1073-1081. doi:10.1084/jem.20021603

35. Ortiz-Pérez S, Martínez-Lapiscina EH, Gabilondo I, et al. Retinal periphlebitis is associated with multiple sclerosis severity. *Neurology*. 2013;81(10):877-881. doi:10.1212/WNL.0b013e3182a3525e

36. Misgeld T, Kerschensteiner M, Bareyre FM, Burgess RW, Lichtman JW. Imaging axonal transport of mitochondria in vivo. *Nat Methods*. 2007;4(7):559-561. doi:10.1038/nmeth1055

37. Gerlach C, Moseman EA, Loughhead SM, et al. The Chemokine receptor CX3CR1 Defines three Antigen-Experienced CD8 T cell subsets with Distinct Roles in immune surveillance and Homeostasis. *Immunity* 2016;45(6):1270-1284. doi:10.1016/j.immuni.2016.10.018

38. Batista NV, Chang Y-H, Chu K-L, Wang KC, Girard M, Watts TH. T cell-Intrinsic CX3CR1 marks the most differentiated effector CD4+ T cells, but is largely dispensable for CD4+ T cell responses during chronic viral Infection. *Immunohorizons*. 2020;4(11):701-712. doi:10.4049/immunohorizons.2000059

39. Cordano C, Werneburg S, Abdelhak A, et al. Synaptic injury in the inner plexiform layer of the retina is associated with progression in multiple sclerosis. *Cell Rep Med*. 2024;5(4):101490. doi:10.1016/j.xcrm.2024.101490

40. Marenna S, Huang S-C, Castoldi V, et al. Functional evolution of visual involvement in experimental autoimmune encephalomyelitis. *Mult Scler J Exp Transl Clin*. 2020;6(4):2055217320963474. doi:10.1177/2055217320963474

41. Sekyi MT, Lauderdale K, Atkinson KC, et al. Alleviation of extensive visual pathway dysfunction by a remyelinating drug in a chronic mouse model of multiple sclerosis. *Brain Pathol* . 2021;31(2):312-332. doi:10.1111/bpa.12930

42. Manogaran P, Samardzija M, Schad AN, et al. Retinal pathology in experimental optic neuritis is characterized by retrograde degeneration and gliosis. *Acta Neuropathol Commun*. 2019;7(1):116. doi:10.1186/s40478-019-0768-5

43. Knier B, Rothhammer V, Heink S, et al. Neutralizing IL-17 protects the optic nerve from autoimmune pathology and prevents retinal nerve fiber layer atrophy during experimental autoimmune encephalomyelitis. *J Autoimmun*. 2015;56:34-44. doi:10.1016/j.jaut.2014.09.003

44. Leitgeb RA, Werkmeister RM, Blatter C, Schmetterer L. Doppler optical coherence tomography. *Prog Retin Eye Res*. 2014;41(100):26-43. doi:10.1016/j.preteyeres.2014.03.004

45. Wicklein R, Yam C, Noll C, et al. The OSCAR-MP Consensus Criteria for quality assessment of retinal optical coherence tomography angiography. *Neurol Neuroimmunol Neuroinflamm*. 2023;10(6):e200169. doi:10.1212/NXI.0000000000200169

46. Sidiqi A, Wahl D, Lee S, et al. In vivo retinal fluorescence imaging with curcumin in an Alzheimer mouse model. *Front Neurosci*. 2020;14:713. doi:10.3389/fnins.2020.00713

47. Normando EM, Davis BM, De Groef L, et al. The retina as an early biomarker of neurodegeneration in a rotenone-induced model of Parkinson's disease: evidence for a neuroprotective effect of rosiglitazone in the eye and brain. *Acta Neuropathol Commun*. 2016;4(1):86. doi:10.1186/s40478-016-0346-z

48. Jeon J, Kim S-H, Kong E, et al. Establishment of the reproducible branch retinal artery occlusion mouse model and intravital longitudinal imaging of the retinal CX3CR1-GFP+ cells after spontaneous arterial recanalization. *Front Med (Lausanne)*. 2022;9:897800. doi:10.3389/fmed.2022.897800

49. Zhang P, Zam A, Jian Y, et al. In vivo wide-field multispectral scanning laser ophthalmoscopy-optical coherence tomography mouse retinal imager: longitudinal imaging of ganglion cells, microglia, and Muller glia, and mapping of the mouse retinal and choroidal vasculature. *J Biomed Opt*. 2015;20(12):126005. doi:10.1117/1.JBO.20.12.126005

50. Miller EB, Zhang P, Ching K, Pugh EN, Burns ME. In vivo imaging reveals transient microglia recruitment and functional recovery of photoreceptor signaling after injury. *Proc Natl Acad Sci U S A*. 2019;116(33):16603-16612. doi:10.1073/pnas.1903336116